



**HAL**  
open science

## Probing GLIMPSE Extended Green Objects (EGOs) with hydroxyl masers

O. S. Bayandina, P. Colom, S. E. Kurtz, N. N. Shakhvorostova, I. E. Val'Tts

► **To cite this version:**

O. S. Bayandina, P. Colom, S. E. Kurtz, N. N. Shakhvorostova, I. E. Val'Tts. Probing GLIMPSE Extended Green Objects (EGOs) with hydroxyl masers. *Monthly Notices of the Royal Astronomical Society*, 2020, 499, pp.3961-3975. 10.1093/mnras/staa2885 . insu-03715003

**HAL Id: insu-03715003**

**<https://insu.hal.science/insu-03715003>**

Submitted on 8 Dec 2023

**HAL** is a multi-disciplinary open access archive for the deposit and dissemination of scientific research documents, whether they are published or not. The documents may come from teaching and research institutions in France or abroad, or from public or private research centers.

L'archive ouverte pluridisciplinaire **HAL**, est destinée au dépôt et à la diffusion de documents scientifiques de niveau recherche, publiés ou non, émanant des établissements d'enseignement et de recherche français ou étrangers, des laboratoires publics ou privés.

# Probing GLIMPSE Extended Green Objects (EGOs) with hydroxyl masers

O. S. Bayandina<sup>1</sup>,<sup>1,2</sup>★ P. Colom,<sup>3</sup> S. E. Kurtz,<sup>4</sup> G. M. Rudnitskij,<sup>†</sup> N. N. Shakhvorostova<sup>2</sup> and I. E. Val'tts<sup>2</sup>★

<sup>1</sup>Joint Institute for VLBI ERIC, Oude Hoogeveensedijk 4, NL-7991 PD Dwingeloo, the Netherlands

<sup>2</sup>Astro Space Center, P.N. Lebedev Physical Institute of RAS, 84/32 Profsoyuznaya st., Moscow 117997, Russia

<sup>3</sup>LESIA, Observatoire de Paris-Meudon, CNRS, UPMC, Université Paris-Diderot, 5 place Jules Janssen, Meudon F-92195, France

<sup>4</sup>Instituto de Radioastronomía y Astrofísica, Universidad Nacional Autónoma de México, Apdo. Postal 3-72, Morelia 58089, Mexico

Accepted 2020 September 15. Received 2020 September 11; in original form 2019 August 12

## ABSTRACT

We present a study of 18 cm OH maser emission toward 20 high-mass young stellar object outflow candidates (Extended Green Objects, EGOs) identified from the Spitzer Galactic Legacy Infrared Mid-Plane Survey Extraordinaire (GLIMPSE). All four OH ground state lines at 1612, 1665, 1667, and 1720 MHz, together with 20-cm continuum emission, were observed with the Karl G. Jansky Very Large Array C-configuration. Follow-up polarimetric single-dish observations with the Nançay radio telescope were performed for the same OH transitions, except 1612 MHz. OH maser emission is found to be an uncommon feature of the sample, with a 50 per cent detection rate for the entire sample and a  $\sim 44$  per cent detection rate for the ‘likely’ EGOs. No 20-cm continuum emission is detected toward any of the sources. In most cases, the detected OH maser emission arises in vicinity to compact central sources; OH masers coexist with the 6.7 GHz methanol masers, but are found in more diffuse and extended halo-shaped regions of several thousand astronomical units in size. Comparing EGO samples with OH maser detection and non-detection, EGOs showing OH maser emission tend to have lower dust clump masses, but higher 24 and 4.5  $\mu\text{m}$  flux densities. Thus, OH maser emission might be an indicator of more evolved EGOs, since strong compact mid-infrared emission in the absence of compact radio continuum emission is thought to be associated with the later stage of massive star formation.

**Key words:** masers – polarization – stars: formation – stars: massive.

## 1 INTRODUCTION

Massive stars as the source of ultraviolet radiation, turbulent energy, and heavy elements play a key role in galactic evolution (e.g. Zinnecker & York 2007; Heckman & Thompson 2017). However, the early stages of massive star formation remain a debatable question, mostly because of observational difficulties: massive young stellar objects (MYSOs) are rare, evolve quickly, hardly ever form in isolation and are deeply embedded in their parent clouds (Zinnecker & York 2007).

The study of MYSOs at a pre-hypercompact (HC)/ultracompact (UC) H II region stage plays a crucial role in the development of massive star formation theory. The discovery of features typical for low-mass stars in MYSOs (circumstellar discs, jets, and disc-mediated accretion bursts) strongly supports the Core Accretion scenario of massive star formation (e.g. Shu, Adams & Lizano 1987; McKee & Tan 2003) and opposes the Competitive Accretion scenario (Bonnell, Bate & Zinnecker 1998; Bally & Zinnecker 2005).

Recently, a promising new sample of MYSO candidates was selected from *Spitzer Space Telescope* data. Cyganowski et al. (2008) catalogued over 300 sources with extended 4.5  $\mu\text{m}$  emission in the *Spitzer* GLIMPSE-I survey images (Benjamin et al. 2003; Churchwell et al. 2009). The 4.5- $\mu\text{m}$  band of the *Spitzer Space Telescope*'s

InfraRed Array Camera (IRAC, Fazio et al. 2004) was chosen because it contains shock-excited molecular line emission associated with active protostellar outflows (e.g. de Buizer & Vacca 2010, and references therein) and lacks polycyclic aromatic hydrocarbon (PAH) emission (see fig. 1 in Reach et al. 2006). According to colour coding of IRAC images the 4.5- $\mu\text{m}$  band is ‘green’, and objects of the new MYSO sample are named ‘Extended Green Objects’ (EGOs, Cyganowski et al. 2008).

The EGO sample has been widely studied in outflow tracer lines: HCO<sup>+</sup>, CO, SiO (Cyganowski et al. 2009, 2011b; He, Takahashi & Chen 2012), H<sub>2</sub> (Lee et al. 2012), and in outflow-associated maser lines: Class I CH<sub>3</sub>OH masers (cIMM, Towner et al. 2017; Cyganowski et al. 2009; Chen et al. 2013) and H<sub>2</sub>O masers (Cyganowski et al. 2013; Rudnitskii et al. 2016). Meanwhile, less attention has been paid to the outflow excitation area and the nature of the driving sources. About two dozen sources were observed in the continuum at 1.3 and 3.6 cm (Cyganowski et al. 2011a; Towner et al. 2017) and in Class II 6.7-GHz CH<sub>3</sub>OH maser (cIIMM) lines (Cyganowski et al. 2009). EGOs were searched for 3-mm molecular line emission in an attempt to find infall signatures (Chen et al. 2010).

A potentially promising step in the investigation of EGOs is OH maser observations. OH masers are widespread and known to be associated not only with UCH II regions (e.g. Garay & Lizano 1999), but also with the earlier stage of molecular outflows and circumstellar discs (e.g. Edris, Fuller & Cohen 2007, and references therein). High spatial and spectral resolution observations of OH masers allow us to

\* E-mail: bayandina@jive.eu (OSB); ivaltts@asc.rssi.ru (IEV)

† Deceased August 13, 2020.

**Table 1.** EGO sample observation parameters.

Source	Frequency (MHz)	VLA observations				NRT observations		
		Beam (arcsec × arcsec)	PA (°)	rms (Jy beam <sup>-1</sup> )	Detect. <sup>a</sup>	Number of chans	Integ. Time (min)	Detect. <sup>a</sup>
G19.36–0.03	1612	18.35 × 11.19	18.64	0.02	–	n.o.	n.o.	n.o.
	1665	18.47 × 10.69	23.53	0.02	+	512	12	+
	1667	17.97 × 10.89	19.65	0.03	+	512	12	+
	1720	17.41 × 10.97	20.15	0.03	–	512	16	–
G23.01–0.41	1612	17.59 × 11.60	16.83	0.02	–	n.o.	n.o.	n.o.
	1665	16.81 × 10.97	13.67	0.02	+	512	8	+
	1667	17.15 × 11.28	13.83	0.02	+	512	8	+
	1720	17.77 × 11.52	31.23	0.02	–	512	8	abs
G24.94+0.07	1612	16.27 × 11.21	10.36	0.03	+	n.o.	n.o.	n.o.
	1665	16.21 × 10.95	16.02	0.02	+	512	8	+
	1667	15.73 × 10.78	9.18	0.03	–	512	8	therm/abs
	1720	15.21 × 10.78	–169.78	0.03	–	512	4	therm
G28.83–0.25	1612	32.41 × 11.22	–50.58	0.03	–	n.o.	n.o.	n.o.
	1665	31.47 × 11.18	–49.57	0.03	+	512	12	+
	1667	30.67 × 11.53	–51.29	0.04	+	512	12	+
	1720	30.37 × 10.86	–50.28	0.04	–	512	12	abs
G34.40+0.23	1612	29.76 × 11.52	–52.32	0.03	+	n.o.	n.o.	n.o.
	1665	28.48 × 11.15	–52.93	0.02	+	1024	8	+
	1667	28.92 × 12.85	–52.15	0.02	+	1024	8	+
	1720	27.84 × 10.96	–52.67	0.03	–	512	8	therm
G35.03+0.35	1612	27.11 × 11.64	–52.27	0.03	–	n.o.	n.o.	n.o.
	1665	26.81 × 11.42	–56.50	0.02	+	1024	12	+
	1667	26.05 × 11.40	–52.85	0.03	+	512	12	+
	1720	25.58 × 10.96	–52.15	0.02	–	512	8	abs
G35.20–0.74	1612	26.02 × 11.65	–51.13	0.03	–	n.o.	n.o.	n.o.
	1665	26.26 × 11.68	–55.12	0.03	+	1024	8	+
	1667	28.18 × 12.52	–63.87	0.03	+	512	8	+
	1720	24.57 × 11.02	–51.74	0.03	–	512	8	therm/abs
G43.04–0.45	1612	13.31 × 11.62	13.09	0.03	–	n.o.	n.o.	n.o.
	1665	12.83 × 10.76	–172.57	0.02	+	512	8	+
	1667	12.99 × 10.89	–174.16	0.02	+	512	8	+
	1720	12.51 × 10.66	12.72	0.02	–	512	8	–
G45.47+0.07	1612	13.13 × 11.41	–174.14	0.03	–	n.o.	n.o.	n.o.
	1665	12.83 × 11.02	–0.17	0.02	+	1024	12	+
	1667	13.53 × 11.23	21.34	0.02	+	512	12	+
	1720	12.06 × 11.41	–178.61	0.02	+	512	4	+
G45.47+0.13	1612	13.15 × 11.38	–173.10	0.02	–	n.o.	n.o.	n.o.
	1665	12.83 × 11.03	–0.13	0.03	+	512	16	+
	1667	13.33 × 10.89	18.85	0.03	+	512	16	+
	1720	12.07 × 11.41	–175.43	0.03	–	512	8	abs

Notes: <sup>a</sup>Detection summary of VLA and NRT observations: ‘–’ – non-detection, ‘+’ – detection of maser line, ‘therm’ – detection of thermal line, ‘abs’ – detection of absorption line, and ‘n.o.’ – not observed.

investigate the structure, kinematics and magnetic field configuration of the inner regions of the source, that is, outflow ejection regions. Analysis of magnetic fields in the disc area is crucial to understand the outflows’ origin.

To study properties of OH maser emission in the EGO sample, we conducted single-dish and interferometric observations. Our first single-dish survey of OH maser emission in the direction of EGOs was to search for outflow associated 1720 MHz OH masers (Litovchenko et al. 2012). The survey found a very high detection rate of 72 per cent for OH(1720) emission in the direction of EGOs. As a follow-up to the single-dish survey, we observed 20 EGOs with the Karl G. Jansky Very Large Array (VLA) in all four ground-state OH lines. An overview of the observations and first statistical results were reported in Bayandina, Val’tts & Kurtz (2015). In the direction of 20 EGOs, maser emission at 1665/1667 MHz was detected in ~50 per cent of the sample. To improve upon our OH polarimetric data, we performed additional high-spectral resolution

single-dish observations with the radio telescope at Nançay (France). The receiving equipment of this radio telescope allows simultaneous observations of all four Stokes parameters.

In this paper, we discuss in more detail the spatial distribution and polarimetric properties of OH masers detected in EGO sources.

## 2 OBSERVATIONS AND DATA REDUCTION

### 2.1 The Karl G. Jansky Very Large Array

Continuum and spectral line observations of the EGO sample were carried out in 2013 July–August using the VLA C-configuration with an angular resolution of about 16 arcsec. A summary of the sample and observational parameters is given in Table 1.

The sample consists of 10 EGOs detected in OH maser lines. All sources are taken from the EGO catalogue of Cyganowski et al. (2008). Most of the sources are defined as ‘likely’ MYSO

**Table 2.** OH maser parameters obtained with the VLA in the EGO sample.

Source	Trans. (MHz)	Pol.	RA(J2000) (h m s)	Dec.(J2000) ( $^{\circ}$ ' ")	Integrated flux (Jy)	Peak flux (Jy beam $^{-1}$ )	$V_{LSR}$ (km s $^{-1}$ )
G19.36–0.03	1665	R	18:26:25.757 $\pm$ 0.007	–12:03:53.79 $\pm$ 0.19	2.81 $\pm$ 0.09	2.60 $\pm$ 0.05	20.94
			18:26:25.764 $\pm$ 0.003	–12:03:53.70 $\pm$ 0.09	5.53 $\pm$ 0.09	5.46 $\pm$ 0.05	21.29
			18:26:25.758 $\pm$ 0.003	–12:03:53.81 $\pm$ 0.09	3.64 $\pm$ 0.06	3.65 $\pm$ 0.03	21.64
			18:26:25.771 $\pm$ 0.012	–12:03:53.61 $\pm$ 0.29	0.87 $\pm$ 0.05	0.99 $\pm$ 0.03	21.99
			18:26:25.728 $\pm$ 0.021	–12:03:54.94 $\pm$ 0.57	0.65 $\pm$ 0.06	0.58 $\pm$ 0.03	22.35

Notes: \* Table 2 is published in its entirety in the machine-readable format. A portion is shown here for guidance regarding its form and content.

outflow candidates, with only two ‘possible’ sources: G43.04–0.45 and G45.47+0.13. The declination cut-off for the sample was set at  $> -30^{\circ}$  to ensure visibility with the VLA.

The continuum data cover the frequency range from 1000 to 2000 MHz and were observed in eight spectral windows, each one with 64 2-MHz channels. About 30 per cent of the channels were affected by RFI (radio-frequency interference) and their data were flagged before imaging. The typical noise level in the images is about 1 mJy beam $^{-1}$ .

The spectral line observations consist of all four hyperfine transitions of the ground rotational state of the OH molecule at frequencies of 1612, 1665, 1667, and 1720 MHz. There were four spectral windows (one for each spectral line) with a bandwidth of 1 MHz and 512 channels, corresponding to a velocity range of 170 km s $^{-1}$  and a velocity resolution of 0.34 km s $^{-1}$ .

The absolute amplitude calibrators were 3C 286 and 3C 48; the phase calibrators were J1822–0938, J1824+1044, and J1833–2103. The integration time for each EGO was about 8 min on-source. Observations were made in the full polarization mode.

Calibration, imaging, and data analysis were performed using the NRAO software package CASA (Common Astronomy Software Applications: <http://casa.nrao.edu>, McMullin et al. 2007). Data were calibrated with the CASA package ‘VLA calibration pipeline’, which is currently designed to work for Stokes  $I$  continuum data, so the standard calibration process was modified to accommodate spectral line data. We excluded the procedure that searches for and flags RFI in the target source data, as this process may remove spectral lines; the RFI search was done manually. To avoid loss in spectral resolution, Hanning smoothing was not performed.

The process of imaging differs slightly from that used in Bayandina et al. (2015). Imaging of continuum and spectral data were performed with the Clark CLEAN algorithm (Clark 1980); the process was automated with PYTHON scripts. ‘Briggs’ weighting was used to obtain the optimal combination of resolution and sensitivity (note that in Bayandina et al. (2015) we used natural weighting because our primary goal was to search for weak OH(1720) emission). First, for each source we searched for emission over a large area of the sky (up to 32 arcmin  $\times$  32 arcmin) in Stokes  $I$  maps. Then the final maps were prepared with area coverage 320 arcsec  $\times$  320 arcsec for OH spectral lines, with separate maps for right- (RCP) and left-circular polarization (LCP). The images were cleaned (CASA task ‘CLEAN’) to a flux limit of twice the theoretical noise level.

OH data were not self-calibrated because the images were close to the theoretical noise limit (about 25–30 mJy beam $^{-1}$ ) and test self-calibration improved the signal-to-noise ratio by less than a factor of about 2.

A 2D Gaussian brightness distribution was fitted to every channel of an OH map (CASA task ‘IMFIT’) with a flux density above the  $5\sigma$  level to determine absolute positions and flux densities (integrated and peak) of the maser features. Emission caused by

spectral ringing or spatial sidelobes of the synthesized beam from other (stronger) features were excluded from consideration. The fit results are summarized in Table 2.

OH spectra were obtained with the CASA Spectral Profile Tool by plotting for each spectral channel the flux density within a region with size from 30 arcsec  $\times$  30 arcsec up to 60 arcsec  $\times$  60 arcsec (depending on the beam position angle) centred on the emission centroid.

## 2.2 Nançay decimetric radio telescope

For the 10 EGOs detected in OH lines with the VLA, polarimetric observations at frequencies of 1665, 1667, and 1720 MHz were made during the period of 2015 August–November with the Nançay radio telescope (NRT).

The NRT has a collecting area of 200  $\times$  34.5 m and a half-power beamwidth (HPBW) of 3.5 arcmin  $\times$  19 arcmin at 18 cm in right ascension and declination, respectively. Four linear polarization and two circular modes are used to measure the full polarization of the OH maser emission. The NRT uses two orthogonal linearly polarized feeds. First, vertical and horizontal polarizations (position angles  $L0^{\circ}$  and  $L90^{\circ}$ ) are observed. Then, the feeds are rotated by  $45^{\circ}$ , and linear polarizations with angles  $45^{\circ}$  and  $-45^{\circ}$  are observed. To get circular polarization spectra, high-frequency phase shifters are employed, advancing and retarding the two orthogonal linear-polarization signals by  $\pi/2$ . The shifted signals are combined to obtain two circularly polarized modes – RCP and LCP. All 1024-channel spectra are recorded separately. Finally, the four Stokes parameters are calculated from  $I = L0^{\circ} + L90^{\circ}$ ,  $Q = L0^{\circ} - L90^{\circ}$ ,  $U = L45^{\circ} - L-45^{\circ}$ , and  $V = RC - LC$ . Thus, the full polarization pattern of the OH maser emission is produced.

Strong emission-line sources were observed using all 1024 channels. Weak-line sources were observed using a frequency-modulation technique. They were observed in two 512-channel bands which were then folded, providing a  $\sqrt{2}$  improvement in the signal-to-noise ratio. As with the VLA observations, the integration time on-source was  $\sim 8$  min. For more details, see Table 1. The sensitivity for a point source at  $0^{\circ}$  declination is 1.4 K Jy $^{-1}$ . The spectral resolution of these observations is 0.07 km s $^{-1}$ .

Generic NRT observations and data processing are described in detail, for example, in Szymczak & Gerard (2004), Slysh et al. (2010), and Bayandina, Alakoz & Val’ts (2013).

## 3 RESULTS

### 3.1 Comparison of the NRT and VLA data

The spectra for all sources obtained in 2013 using the VLA and in 2015 using the NRT are presented in Fig. 1. There are two panels, with the single-dish NRT spectrum and the cross-correlation VLA

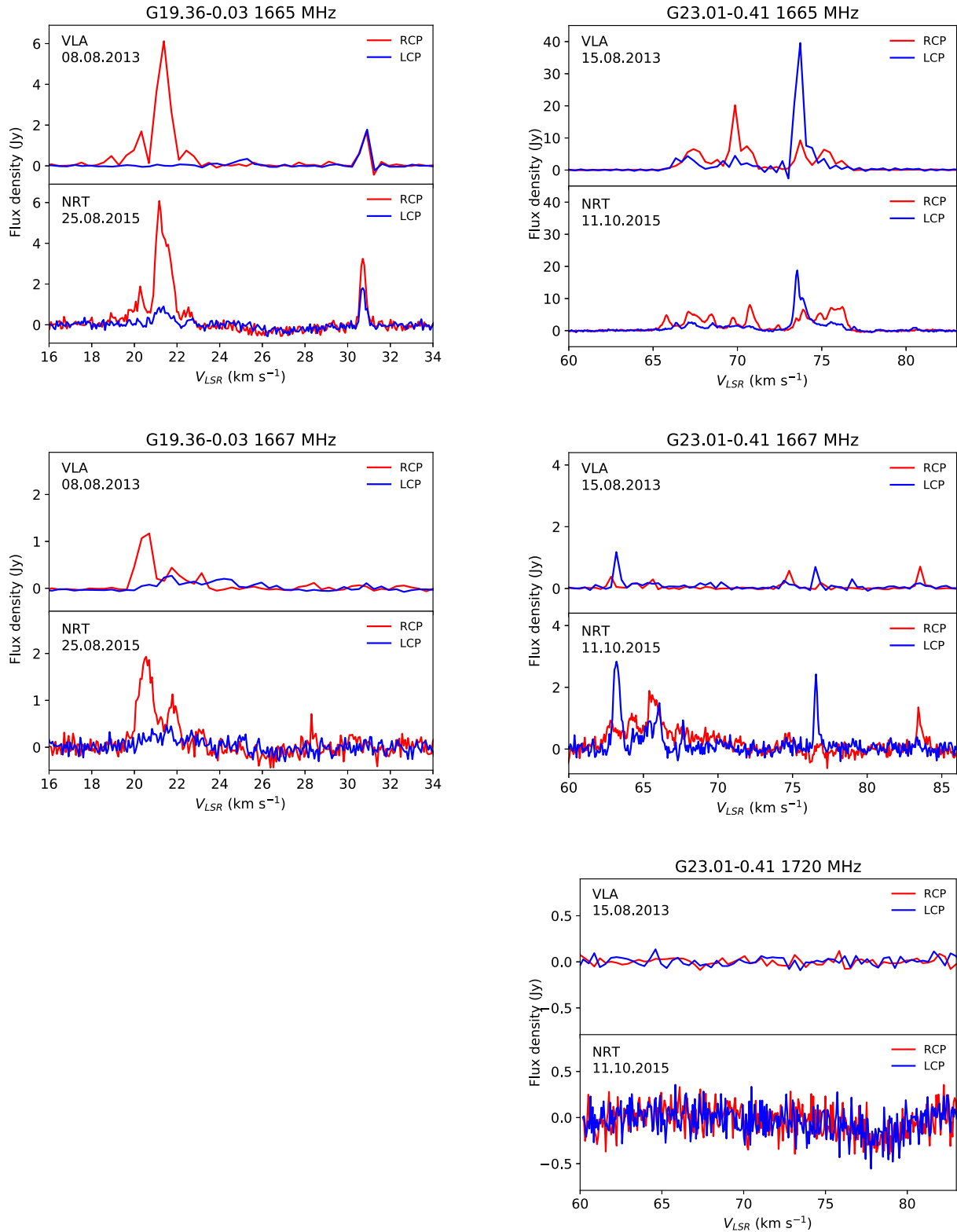


**Figure 1.** Spectra of EGO sources obtained with VLA (upper panel) and NRT (bottom panel). Facility and date of observation are listed in the upper left corner of each spectral panel. LCP indicated in blue and RCP – in red. *Note:* Sample of Figure 1, the full version is available online.

spectrum for every detected OH transition in each source. For cases in which a broad thermal line or absorption line was detected with the NRT, the VLA panel shows the noise spectrum (i.e. the non-detection) of the interferometric data. Facility and date of observation

are shown in the upper left corner of each panel. The red and blue lines indicate RCP and LCP emission, respectively.

Comparison of NRT single-dish spectra and VLA cross-correlation spectra was done assuming that OH maser flux is

fully recovered in VLA C-configuration observations (see Section 3.2).

The higher spectral resolution ( $0.07 \text{ km s}^{-1}$ ) of the NRT observations shows that in many cases the spectral lines detected with the VLA are blends of distinct velocity components; see, for example, the spectra of G35.20–0.74 and G43.04–0.452.

Comparison of the OH lines at the two observation epochs did not reveal a significant variability in the sources. No new spectral features were detected with the NRT. For most sources, the NRT spectra show higher flux densities than those observed with the VLA. However, this lower flux may be a resolution effect, resulting from the big difference in the spectral resolution of the NRT ( $0.07 \text{ km s}^{-1}$ ) and the VLA ( $0.34 \text{ km s}^{-1}$ ). Moreover, there is a big difference in the sizes of the NRT and VLA beams. The NRT ( $3.5 \text{ arcmin} \times 19 \text{ arcmin}$ ) covers a much larger solid angle, which may include maser emission that is spatially resolved by the VLA beam ( $\sim 20 \text{ arcsec} \times 10 \text{ arcsec}$ ). The most striking example is G34.40+0.23, the only source showing significantly different VLA and NRT spectra. This source falls into the NRT beam together with supernova remnant G34.3+0.2 (W44). The bright lines at  $\sim 55\text{--}60 \text{ km s}^{-1}$  are associated with W44 rather than with G34.40+0.23.

### 3.2 VLA: OH maser spatial distribution and kinematics

The position, velocity, and flux density (integrated and peak) for each maser feature detected with the VLA in RCP and LCP data cubes are presented in Table 2 (note that in Bayandina et al. (2015) only spectral line peak data were listed).

The formal uncertainty in the position of a spectrally isolated and spatially unresolved peak caused by thermal noise in an interferometric image is

$$\sigma_{\theta} = 0.5 \vartheta_b \sigma_S / S, \quad (1)$$

where  $\vartheta_b$ ,  $\sigma_S$ , and  $S$  are the synthesized beam size, and the rms, and peak flux density, respectively (Reid et al. 1988). Table 1 gives the synthesized full width at half-maximum beam size and rms noise levels in the VLA maps for all sources (these differ from Bayandina et al. 2015 due to a different approach to the data processing, see Section 2.1). The synthesized beams become very elongated at low declination because of short projected N–S ( $u, v$ )-coverage, for example, 20 arcsec (see Table 1). With a typical noise level of 0.03 Jy, one obtains a formal fitting error of  $\sim 0.3 \text{ arcsec}$  for a 1 Jy peak. Following these estimates, we present three decimal places for the right ascension coordinate and two for declination. The position error in the E–W direction is usually smaller (by a factor of  $\sim 2$ ) than in the N–S direction. Note that in most cases the flux density of OH 1612/1667/1720 MHz emission is lower than that of 1665 MHz. Positional uncertainties for maser spots with a low flux density can be much higher (equation 1), which can lead to a visual extension of a maser cluster.

We use term ‘maser spot’ to refer to an individual emission peak position in each velocity channel, listed in Table 2. But note that with the VLA C-configuration spatial (Table 1) and spectral resolution ( $\sim 0.34 \text{ km s}^{-1}$ ), most of the maser spots appear to be unresolved and spectrally blended (see Fig. 1). OH maser spots are known to have a size of  $\sim 10 \text{ au}$  (e.g. Elitzur et al. 1992), which is  $\sim 0.005 \text{ arcsec}$  at the distance of  $\sim 2 \text{ kpc}$  (the closest distance for our sample – see Table 3).

The spatial structures of OH maser clusters in each source, based on the positions and velocities reported in Table 2, are plotted in Fig. 2. Maser spots in the left-hand polarization are represented by circles and in right-hand polarization by triangles. To show the

kinematics, we colour the maser spots according to their velocities. Each map is accompanied by spectra, which show the flux densities of the plotted OH features.

To study the detected OH masers in the context of their host regions, we compared positions of OH masers, methanol masers, and their continuum counterpart. Combined maps of the observed regions are presented in Fig. 4. Methanol maser data as well as data on continuum counterparts is taken from Cyganowski et al. (2009) and Hu et al. (2016). Cyganowski et al. (2009) is chosen because it targets the EGO sample, and because it provides information on both the 6.7 GHz methanol maser emission (tracing the protostar vicinity) and on the 44 GHz methanol maser emission (tracing the surrounding gas shocked by outflows). Data on EGO sources not studied in Cyganowski et al. (2009) are taken from Hu et al. (2016). The origin of the information on the direction of large-scale outflow in each source is given in Section 4.

### 3.3 VLA: 20 cm continuum emission

Continuum emission at 20 cm was not detected in the direction of any of the 10 EGOs of our sample at a  $5\sigma$  level of  $5 \text{ mJy beam}^{-1}$ . We searched the VLA images for continuum emission in the vicinity of the extended  $4.5 \mu\text{m}$  emission – typically in a region of  $\sim 1 \text{ arcmin}$  diameter. More distant 20 cm continuum sources are present in the images for some fields in a  $\sim 2 \text{ arcmin}$  diameter area.

### 3.4 NRT: polarization parameters and spectra

Results of the NRT full polarization observations of 10 OH masers in the direction of EGOs are summarized in Fig. 3. Data on the  $I$ ,  $Q$ ,  $U$ , and  $V$  Stokes parameter profiles, linearly polarized flux density ( $p$ ), degree of circular ( $m_C$ ), and linear polarization ( $m_L$ ), and polarization position angle ( $\chi$ ) are presented. All detected OH masers show circularly polarized features, while linearly polarized features are found in 80 per cent of the 1665-MHz masers and 50 per cent of the 1667-MHz masers. Linear polarization is always accompanied by circular polarization; that is, elliptically polarized profiles are observed.

In the absence of significant differences between the structure of NRT and VLA spectra (see Fig. 1), the polarimetric data obtained with the NRT were attributed to the VLA-detected maser feature of corresponding velocity. However, note that the NRT and VLA data are obtained with significantly different beams. OH emission detected with NRT may come from regions more extended than VLA maser spots. Thus, our results are most likely affected by spatial blending and averaging of polarization parameters, and they should be considered as estimates. The flux density of Stokes parameters, the median value of circular/linear polarization degree and the median polarization angle across the spectrum of each OH maser detail associated with the spectral line peak are listed in Table 4.

## 4 INDIVIDUAL SOURCES

The following notes contain detailed information on individual sources which are used later in Section 5.

### 4.1 G19.36–0.03

OH masers detected in our survey closely coincide with the cIIMM position (Cyganowski et al. 2009) – see Fig. 4. OH and 6.7 GHz methanol maser clusters have about the same size of  $\sim 1 \text{ arcsec}$  or  $\sim 2000 \text{ au}$  (assuming the distance to the source). OH and 6.7 GHz methanol masers do not coincide with the position of the  $24 \mu\text{m}$  EGO

**Table 3.** Properties of EGO subsamples with OH maser detections and non-detections.

Source	EGO <sup>a</sup>	IRDC <sup>a</sup>	Integrated Flux <sup>a</sup> (Jy)		Clump mass <sup>b</sup> (M <sub>⊙</sub> )	Distance <sup>c</sup> (kpc)
			24 μm	4.5 μm		
OH maser detections						
G19.36−0.04	2	Y	–	0.1	438 <sup>+342</sup> <sub>−236</sub>	2.09 <sup>+0.48</sup> <sub>−0.54</sub>
G23.01−0.41	1	N	6.2	0.2	4024 <sup>+1514</sup> <sub>−1114</sub>	4.59 <sup>+0.38</sup> <sub>−0.33</sub>
G24.94+0.07	1	N	1.4	0.06	126 <sup>+76</sup> <sub>−54</sub>	2.77 <sup>+0.37</sup> <sub>−0.40</sub>
G28.83−0.25	1	Y	3.6	0.2	1465 <sup>+511</sup> <sub>−401</sub>	4.88 <sup>+0.34</sup> <sub>−0.33</sub>
G34.40+0.23	1	Y	6.2	0.02	688 <sup>+244</sup> <sub>−186</sub>	1.56 <sup>+0.12</sup> <sub>−0.11</sub>
G35.03+0.35	1	N	<i>10.2</i>	0.5	814 <sup>+385</sup> <sub>−285</sub>	3.24 <sup>+0.39</sup> <sub>−0.39</sub>
G35.20−0.74	1	N	<i>31.7</i>	1.1	–	2.19 <sup>+0.24</sup> <sub>−0.20</sub>
G43.04−0.45	4	N	–	0.01	295 <sup>+191</sup> <sub>−117</sub>	3.89 <sup>+0.65</sup> <sub>−0.54</sub>
G45.47+0.07	1	Y	<i>15.7</i>	0.2	1502 <sup>+961</sup> <sub>−656</sub>	4.77 <sup>+0.85</sup> <sub>−0.85</sub>
G45.47+0.13	4	N	–	0.1	1721 <sup>+1084</sup> <sub>−744</sub>	4.69 <sup>+0.82</sup> <sub>−0.82</sub>
Mean <sup>d</sup>			10.7(3.9)	0.3(0.1)	1107(376)	
OH maser non-detections						
G14.33−0.64	1	Y	4.9	0.05	–	1.12 <sup>+0.14</sup> <sub>−0.11</sub>
G18.67+0.03	1	N	3.9	0.06	4923 <sup>+1265</sup> <sub>−1076</sub>	10.81 <sup>+0.24</sup> <sub>−0.23</sub>
G18.89−0.47	1	Y	0.5	0.03	2266 <sup>+762</sup> <sub>−634</sub>	4.28 <sup>+0.28</sup> <sub>−0.31</sub>
G19.01−0.03	1	Y	3.5	0.3	4997 <sup>+1287</sup> <sub>−1084</sub>	11.54 <sup>+0.29</sup> <sub>−0.27</sub>
G22.04+0.22	1	Y	3.3	0.01	728 <sup>+315</sup> <sub>−247</sub>	3.40 <sup>+0.34</sup> <sub>−0.37</sub>
G23.96−0.11	1	N	1.6	0.2	5206 <sup>+1312</sup> <sub>−1114</sub>	10.76 <sup>+0.28</sup> <sub>−0.27</sub>
G25.27−0.43	1	Y	0.2	0.04	9698 <sup>+2727</sup> <sub>−2281</sub>	11.22 <sup>+0.31</sup> <sub>−0.30</sub>
G37.48−0.10	1	N	1.1	0.02	222 <sup>+134</sup> <sub>−91</sub>	3.59 <sup>+0.43</sup> <sub>−0.42</sub>
G39.10+0.49	1	N	1.4	0.03	29 <sup>+35</sup> <sub>−19</sub>	1.47 <sup>+0.45</sup> <sub>−0.47</sub>
G49.27−0.34	1	Y	8.7	0.7	2642 <sup>+2795</sup> <sub>−1625</sub>	5.48 <sup>+1.76</sup> <sub>−1.76</sub>
Mean <sup>d</sup>			2.9(0.8)	0.1(0.07)	3071(993)	

Notes: <sup>a</sup>EGO Catalogue table number, IRDC association, and data on integrated MIPS 24 μm and IRAC 4.5 μm flux densities from Cyganowski et al. (2008). The errors of the given values of the flux density do not exceed 15 per cent; for exact values of uncertainties, see tables 1–4 of Cyganowski et al. (2008). MIPS 24 μm fluxes indicated as saturated or as upper limits in Cyganowski et al. (2008) are in italics.

<sup>b</sup>Masses of associated BGPS dust clumps calculated in Cyganowski et al. (2013). Listed ranges include upper and lower uncertainty in clump mass, for more details see table 8 of Cyganowski et al. (2013).

<sup>c</sup>Kinematic distances calculated for the EGO sample in Cyganowski et al. (2013). For G14.33−0.64 and G35.20−0.74 not included in the sample of Cyganowski et al. (2013), the distances from Wu et al. (2014) and Zhang et al. (2009) are used, respectively.

<sup>d</sup>The mean value of the parameter for each EGO sub-sample with uncertainty indicated in parentheses.

counterpart and seem to be associated with a less-evolved protostar in the region.

The cIIMM and OH(1665) maser clusters show opposite velocity gradients in the east–west direction: redshifted cIIMM spots are located to the east (Cyganowski et al. 2009), while redshifted OH(1665) spots are located to the west (Fig. 2). The blue- and redshifted OH(1665) maser spots seem to form two spatial clusters in the SE and NW parts of the source, respectively. Blueshifted OH spots show strong RCP at 1665 and 1667 MHz. Spots with RCP are not detected at the 5σ level at 1665 MHz, and only one spot is detected at 1667 MHz.

Red- and blueshifted OH(1665) spectral features are situated almost symmetrically around the systemic velocity of the EGO (Fig. 1), as indicated by the centroid velocity of H<sup>13</sup>CO<sup>+</sup> (Cyganowski et al. 2009). Weak absorption at the systemic velocity of the source is found in the NRT spectrum. The spectral feature at ~30.8 km s<sup>−1</sup> shows strong (~98 per cent) linear polarization (see Table 4 and Fig. 3).

This source is one of 17 EGOs found to have an H<sub>2</sub> outflow (Lee et al. 2013). The faint H<sub>2</sub> emission extends along the SE–NW direction. An arc of 44 GHz methanol masers (Cyganowski

et al. 2009) is located ~5 arcsec along the outflow from the OH position (Fig. 4). The 6.7 GHz methanol maser is thought to indicate the position of a driving source of the outflow (Lee et al. 2013). The presence of only one cIIMM locus suggests that despite the complicated mid-infrared (MIR) morphology there is only one YSO with sufficient mass and at an early enough evolutionary stage to excite cIIMM emission (Cyganowski et al. 2009).

#### 4.2 G23.01−0.41

OH maser emission is detected in the vicinity of a 24 μm EGO counterpart and coincides with a 6.7 GHz methanol maser site (Fig. 4). However, OH maser emission occupies a larger area than the 6.7 GHz methanol maser cluster. Sizes of maser sites are ~5000 and ~2000 au for the OH 1665 MHz and 6.7 GHz methanol, respectively. While the 6.7 GHz methanol maser spots show a clear velocity gradient (Hu et al. 2016), there is no velocity pattern in the distribution of OH(1665) spots (Fig. 2).

One of the most interesting features of OH emission in this source is the much larger extent of OH 1667 MHz emitting region compared

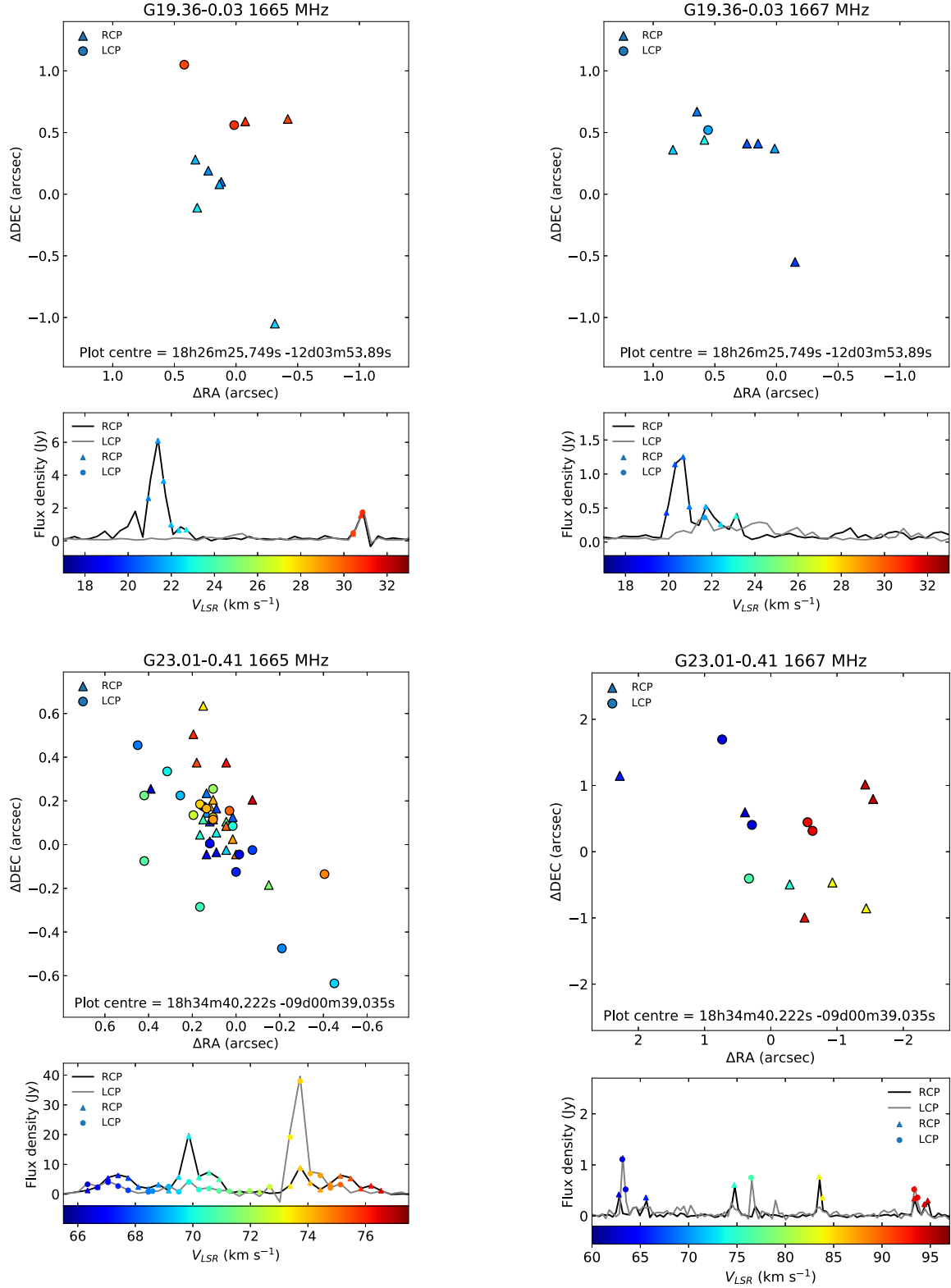


**Figure 2.** Fitted positions of OH masers detected with VLA from Table 2 colour-coded by velocity (see colour bar at the bottom of every panel) and VLA cross-correlation spectra. Triangles represent RCP maser features, while circles show LCP. Position (0,0) represents a geometric centre of 1665 MHz OH maser cluster in each EGO source; corresponding absolute coordinates are listed at the bottom of the map panel. *Note:* Sample of Figure 2, the full version is available online.

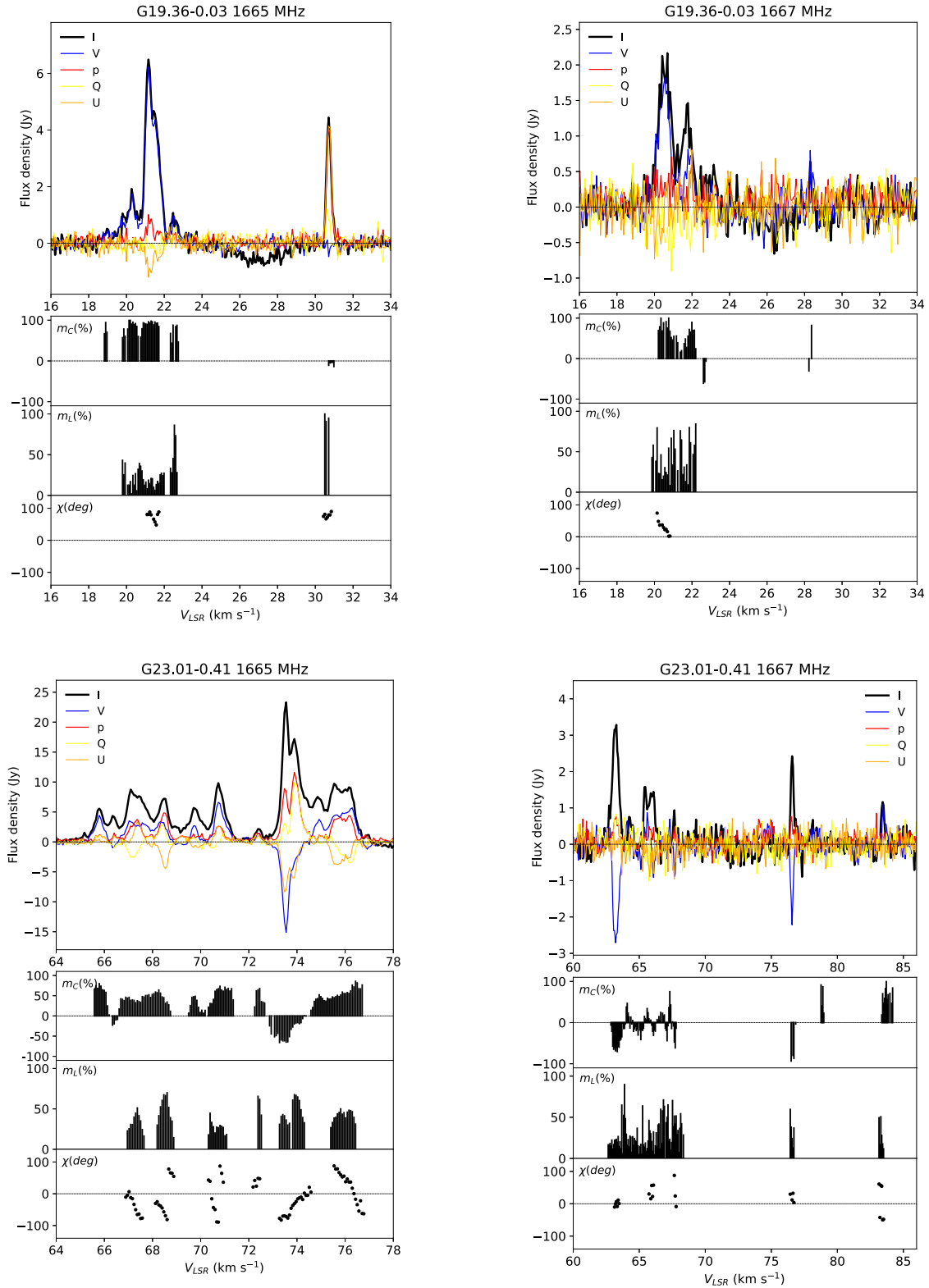


**Figure 3.** Profiles of Stokes parameters (see the legend in the upper left corner for Stokes parameters colour-coding), degree of polarization ( $m_C$  – circular and  $m_L$  – linear) and polarization angle ( $\chi$ ) for the OH lines obtained with NRT in the direction of the EGO sample. *Note:* Sample of Figure 3, the full version is available online.

**Table 4.** OH maser polarization parameters obtained with the NRT in EGO sample.

Source	Trans. (MHz)	$V_{\text{LSR}}$ ( $\text{km s}^{-1}$ )	$I$ (Jy)	$Q$ (Jy)	$U$ (Jy)	$V$ (Jy)	$m_C$ (per cent)	$m_L$ (per cent)	$\chi$ ( $^\circ$ )
G19.36–0.03	1665	21.29	5.11	–0.19	–1.05	4.99	98	21	40
		22.35	0.86	0.16	0.16	0.93	108	26	23
		30.78	4.29	0.80	4.13	–0.18	–4	98	40
	1667	20.60	2.23	–0.77	–0.32	2.09	94	37	11
		21.66	1.39	–0.24	0.3	0.69	50	28	–26
		23.06	0.73	–0.17	–0.18	0.31	42	34	23
G23.01–0.41	1665	66.34	4.35	–0.52	0.39	–0.99	–23	15	–18
		67.40	7.37	–1.55	3.43	2.76	37	51	–33
		69.86	5.26	0.24	–0.85	2.02	38	17	–37
		70.56	6.88	–0.89	1.05	4.18	61	20	–25
		73.73	21.55	3.10	–8.36	–13.25	–61	41	–35
		75.13	7.09	0.28	–0.09	2.92	41	4	–9
G24.94+0.07	1665	36.30	14.60	3.16	9.65	5.28	36	70	36
		41.22	1.13	–0.13	0.51	–0.68	–60	47	–38
		42.28	1.84	–0.06	0.27	1.31	71	15	–39
		42.98	1.78	–0.27	0.43	0.21	12	29	–29
		43.68	1.05	–0.08	0.31	–1.17	–111	30	–38
		79.99	1.63	0.02	–0.01	–1.15	–71	1	–13
G28.83–0.25	1665	81.05	3.02	0.16	0.04	–2.35	–78	5	7
		84.21	3.14	0.20	0.35	2.00	64	13	30
		84.91	6.70	0.66	0.8	5.32	79	15	25
		88.43	2.37	0.09	0.08	2.42	102	5	21
		89.84	3.13	0.69	–0.41	–1.78	–57	26	–15
		94.05	4.11	0.14	–0.05	–3.40	–83	4	–10
G35.03+0.35	1665	47.29	13.56	–1.95	0.20	10.79	80	14	–3
		47.99	50.28	–4.54	–27.2	34.66	69	55	40
		51.16	0.82	–0.31	0.17	–0.86	–105	43	–14
G35.20–0.74	1665	26.10	2.16	1.13	–0.96	0.63	29	69	–20
		26.81	2.37	0.34	–0.32	–1.77	–75	20	–22
		28.21	10.71	0.14	1.65	–8.91	–83	15	43
		28.91	23.12	–4.06	–2.32	7.20	31	20	15
		29.62	6.64	–2.13	3.41	–1.50	–23	61	–29
		30.32	19.29	2.65	0.24	10.56	55	14	3
		34.19	4.73	–0.65	–0.44	3.87	82	17	17
		35.60	2.59	0.36	0.36	–1.03	–40	20	23
		36.65	3.98	0.38	0.82	1.19	30	23	33
		58.08	6.52	–0.06	4.98	3.03	46	76	–45
G43.04–0.452	1665	58.78	0.82	–0.09	–0.14	–0.32	–39	20	29
		60.54	2.31	–0.56	–0.86	–1.43	–62	44	28
		65.34	58.16	–10.97	–10.32	–46.45	–80	26	22
G45.47+0.07	1665	66.04	80.41	39.51	1.11	–38.47	–48	49	1
		67.09	25.22	–0.12	3.60	14.18	56	14	–44
		58.64	15.60	2.26	–1.35	–13.33	–85	17	–15
G45.47+0.13	1665	59.34	23.31	0.76	–2.54	–20.43	–88	11	–37

to OH 1665 MHz. In part, this may be due to larger positional uncertainty of the OH 1667 MHz emission with lower flux density (see equation 1 in Section 3.2). But 1667 MHz emission also shows a much wider velocity range:  $V_{\text{LSR}}(\text{OH } 1667 \text{ MHz}) = 61\text{--}95 \text{ km s}^{-1}$  compared to  $V_{\text{LSR}}(\text{OH } 1665 \text{ MHz}) = 66\text{--}77 \text{ km s}^{-1}$ . There are four OH(1667) spectral feature groups and each group seems to arise in a particular spatial cluster (Fig. 2). A cluster of maser spots with particular velocities (e.g. blueshifted features) has size  $\sim 1$  arcsec ( $\sim 5000$  au), but together they occupy a region of  $\sim 3$  arcsec or  $\sim 14000$  au.

The source shows a complex OH spectrum with strongly polarized RCP and LCP features (Fig. 1). The OH maser emission is blueshifted from the systemic velocity of  $77.4 \text{ km s}^{-1}$  (measured by  $\text{NH}_3$  and  $\text{CH}_3\text{CN}$  lines Codella, Testi & Cesaroni 1997; Furuya et al. 2008). The NRT spectrum at 1720 MHz shows weak absorption at the systemic velocity.

A detailed analysis of the magnetic field structure in the region based on 1665 MHz OH masers was performed by Sanna et al. (2010). Their estimates of the magnetic field strength in the region vary from  $-5.8$  to  $+3.6$  mG.

The source hosts a massive bipolar outflow extended in the NE–SW direction and detected in  $\text{CO}(1-0)$ ,  $^{13}\text{CO}(1-0)$ , and  $\text{HNCO}(5_{05} - 4_{04})$  lines (Furuya et al. 2008). The outflow driving source is located at the position of the 1.3-cm continuum peak (Sanna et al. 2010).

Interferometric VLA and NMA (Nobeyama Millimetre Array) studies in  $\text{NH}_3(3,3)$  (Codella et al. 1997) and  $\text{CH}_3\text{CN}(6-5)$  (Furuya et al. 2008) lines, respectively, indicate the presence of a hot molecular core (HMC). It is thought that the HMC is a flattened structure, rotating around the outflow axis (Furuya et al. 2008). Detection of a rare  $\text{H}_2\text{CO}$  maser at 6 cm suggests a very early stage of evolution of the central source (Araya et al. 2008).

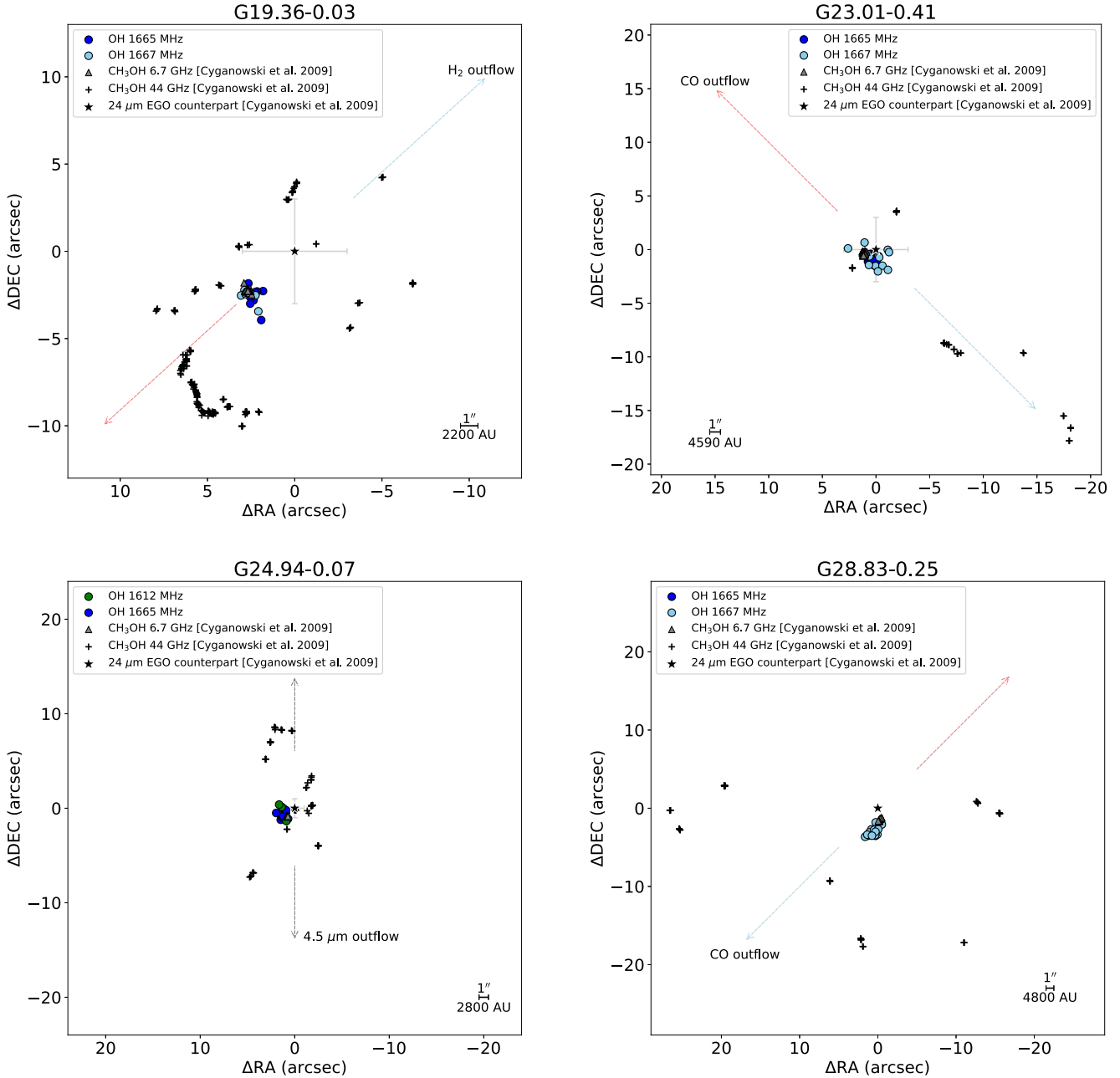


**Figure 4.** Combined maps of objects of the studied EGO sample: OH 1612, 1665, 1667, and 1720 MHz masers – green, blue, light blue, and yellow circles, respectively (this work); CH<sub>3</sub>OH 6.7 GHz masers – grey triangles (Hu et al. 2016; Cyganowski et al. 2009) (see the legend); CH<sub>3</sub>OH 44 GHz masers – black crosses (Cyganowski et al. 2009); 24 μm or C-band counterpart – black star (Cyganowski et al. 2009; Hu et al. 2016) (see the legend); large-scale bipolar outflow – dashed arrows (see Section 4). Dashed arrows indicate the direction, but not the actual position of a bipolar outflow in each source. The physical scale label (in au) assumes the distance to the source listed in Table 3. *Note:* Sample of Figure 4, the full version is available online.

### 4.3 G24.94+0.07

This is one of two sources in our survey that show OH emission at 1612 MHz. Moreover, it is the only source in which OH 1667 MHz emission is *not* detected with the VLA. A weak 1667 MHz line of about 0.4 Jy at  $\sim 35 \text{ km s}^{-1}$  is detected with the NRT along with absorption lines in the redshifted part of the spectrum. The brightest line of the OH(1665) spectrum ( $\sim 9 \text{ Jy}$ ) is blueshifted, while weak lines ( $< 1 \text{ Jy}$ ) have velocities close to the systemic velocity of the cloud.

OH emission at 1665 and 1612 MHz arises from the same region and closely coincides with the 6.7 GHz methanol maser locus. OH

and the 6.7 GHz methanol maser emission are found to the east of the 24 μm EGO counterpart – in the region with the least extent of 4.5 μm emission and the absence of 44 GHz methanol maser emission (Cyganowski et al. 2009). OH(1665) maser emission spreads over a region of  $\sim 1 \text{ arcsec}$  ( $\sim 3000 \text{ au}$ ) with OH(1612) maser spots found on the northern and southern edges of this area (Fig. 2). OH emission in the region is divided into two velocity groups: maser spots with blueshifted velocities ( $V_{\text{LSR}} = 35\text{--}37 \text{ km s}^{-1}$ ) are found in the southeast, and redshifted ones ( $V_{\text{LSR}} = 41\text{--}44 \text{ km s}^{-1}$ ) in the northwest. In contrast, the 6.7 GHz methanol maser emission occupies

a compact region of  $\sim 0.1$  arcsec ( $\sim 300$  au) and a narrow velocity range of  $45\text{--}47$  km s $^{-1}$ .

This MYSO shows signs of both an accretion disc and a bipolar outflow (Cyganowski et al. 2011a).

#### 4.4 G28.83–0.25

This source shows a complex OH spectrum at 1665 and 1667 MHz with a multitude of weak and strongly polarized features. The spectral features are located almost symmetrically with respect to the systemic velocity of the source: features close to the velocity of the system have a strong right-hand polarization, while more distant ones are strongly left-hand-polarized. The 1720-MHz OH spectrum obtained with the NRT shows weak absorption at the systemic velocity.

OH maser emission in the region is found to the north of a  $24\ \mu\text{m}$  source (Cyganowski et al. 2009). The northern part of the OH maser cluster coincides with the 6.7 GHz methanol maser emission site (Fig. 4). The OH maser cluster has a size of  $\sim 1.5$  arcsec ( $\sim 7000$  au), which is about three times larger than the 6.7 GHz methanol maser cluster. Both OH (1665) and OH (1667) clusters are elongated in the SE–NW direction along the large-scale outflow, but neither of them show clear velocity gradients (Fig. 2). This differs from the distribution of the 6.7 GHz maser emission in the region, which has two arcs of maser spots: blueshifted spots are found to the north, and redshifted are found to the south (Cyganowski et al. 2009).

This EGO is located at the edge of the MIR ‘wind-blown bubble’ N49 (Churchwell et al. 2006), between two young sources (a compact H II region to the north and an MYSO to the south) and may represent an example of triggered star formation (Watson et al. 2008). The  $4.5\text{-}\mu\text{m}$  emission traces a bipolar structure, elongated in the east–west direction (Cyganowski et al. 2009). A large-scale outflow was imaged in  $^{13}\text{CO}$  by de Villiers et al. (2014).

#### 4.5 G34.40+0.23

This source shows the strongest OH(1612) maser detected in our survey with a strongly polarized single-peak profile at the systemic velocity of the source (measured by  $\text{C}^{17}\text{O}$ , Giannetti et al. 2014). Main line OH spectra consist of strongly polarized blueshifted features, with only one redshifted feature detected at 1665 MHz (Fig. 1).

OH maser emission at all three detected frequencies arises from the same region of a size  $\sim 1$  arcsec ( $\sim 2000$  au, Fig. 2). The OH maser site in the source does not coincide with either the 6.7 GHz methanol maser emission or the C-band continuum source (Hu et al. 2016) – see Fig. 4.

The high-mass star-forming filamentary cloud G34.4+0.23 was resolved into nine millimetre cores (MM1–MM9) as reported by Rathborne, Jackson & Simon (2006). The OH emission detected in our survey is associated with the MYSO G34.4+0.23 MM1. Shepherd, Nurnberger & Bronfman (2004) conclude that this source is in a very early stage of evolution, based on the presence of warm dust continuum emission at 3 mm and emission in the  $\text{H}^{13}\text{CO}^+$  line, and the lack of NIR emission at  $1.2\text{--}2.1\ \mu\text{m}$ . The source is associated with a massive bipolar outflow oriented in the SE–NW direction (Shepherd et al. 2007). The C-band continuum source from Hu et al. (2016) marks the core MM2, which is an UCH II region (Shepherd et al. 2004, 2007). And the 6.7 GHz methanol maser is associated with the source MM4. Thus, G34.40+0.23 is the only OH maser source of our sample without a 6.7 GHz methanol maser counterpart.

A detailed study of the magnetic field structure in the sky plane by means of linear polarization of dust emission was reported by Cortes et al. (2008). Their observations suggest that field lines are orthogonal to the main axis of the N–S filament hosting G34.4+0.23 MM. This morphology suggests the presence of a flattened disc with the magnetic field along the minor axis, in agreement with the theory of magnetically supported molecular clouds.

#### 4.6 G35.03+0.35

The OH(1665) spectrum shows one bright spectral feature with predominantly right-hand polarization (Fig. 1). The feature is blueshifted from the systemic velocity of  $49.5$  km s $^{-1}$  by about  $1.5$  km s $^{-1}$  (Beltrán et al. 2014). There is weak absorption in the red part of the NRT 1720 MHz spectrum.

OH maser emission in the source is detected in a linear cluster elongated from the  $24\ \mu\text{m}$  EGO counterpart (Cyganowski et al. 2009) to the north (Fig. 4). The OH cluster has a length of  $\sim 1.5$  arcsec ( $\sim 4000$  au) in the NS direction. A 6.7 GHz methanol maser is also found in the vicinity of the  $24\ \mu\text{m}$  source (Cyganowski et al. 2009), but it is separated from the OH site by  $\sim 0.5$  arcsec eastward.

Detected OH emission is associated with the most chemically rich core in the region (core A), which is thought to be the driving source of a bipolar outflow (Beltrán et al. 2014). This source is considered to be one of the most convincing examples of Keplerian discs around a high-mass protostar (Beltrán et al. 2014).

#### 4.7 G35.20–0.74

This source shows rich OH maser spectra with blue- and redshifted spectral features located almost symmetrically with respect to the source velocity of  $\sim 33$  km s $^{-1}$  (Paron & Weidmann 2010). Broad and highly polarized OH 1720 MHz lines in the red part of the NRT spectrum are detected.

OH and the 6.7 GHz methanol maser emission in the source come from the same region of size of  $\sim 2$  arcsec ( $\sim 4000$  au, Fig. 4). Clusters of OH and 6.7 GHz methanol maser emission are elongated in the SE–NW direction, perpendicular to the NE–SW molecular outflow (Little et al. 1983; Matthews et al. 1984). OH maser emission is associated with core B (Sánchez-Monge et al. 2013), which hosts a binary system of UC/HCH II regions surrounded by a Keplerian rotating disc (Beltrán et al. 2016). A massive molecular disc perpendicular to the bipolar outflow was found in CS (Dent et al. 1985) and  $\text{NH}_3$  (Little et al. 1985; Brebner et al. 1987) emission. The location, orientation, and size of the OH maser cluster suggest its association with the molecular disc.

#### 4.8 G43.04–0.45

OH maser emission is detected in the vicinity of a C-band continuum source and is associated with a 6.7 GHz methanol maser (Hu et al. 2016) – see Fig. 4. The diffuse cluster of OH emission closely coincides with the northern lobe of the SE–NW elongated cluster of 6.7 GHz methanol maser emission.

An unusual spatial distribution of OH(1665) masers is found: spots form a roughly bipolar structure, with the NE lobe consisting exclusively of left-hand-polarized maser components, while the SE lobe is exclusively right-hand-polarized.

This source stands out in our sample for the lack of evidence of a bipolar outflow – the only indication of such is the detection of extended  $4.5\ \mu\text{m}$  emission. Observations of the CO and  $\text{H}_2$  lines show no evidence of an outflow (Zhang et al. 2005; Varricatt et al.

2010; Lee et al. 2013). Edris et al. (2017) present the results of main line OH observations with the Multi-Element Radio Linked Interferometer Network (MERLIN) (beam  $0.9 \text{ arcsec} \times 0.4 \text{ arcsec}$ ). They noted that the absence of signatures of a disc, bipolar outflow or H II region indicates a very early evolutionary stage.

#### 4.9 G45.47+0.07

This is the only source in our survey that shows OH 1720 MHz emission. OH maser spectra at all detected frequencies are dominated by LCP features.

OH emission is scattered in the vicinity of the H II region (Wood & Churchwell 1989) in an area of  $\sim 1 \text{ arcsec}$  ( $\sim 8000 \text{ au}$ ). The OH(1665) maser cluster does not show a specific spatial structure or velocity gradient, while the OH(1667) cluster is more extended and flattened in the east-west direction, perpendicular to an outflow (Fig. 2). An active bipolar outflow propagating in the N-S direction was detected by HCO<sup>+</sup> and CO emission (Ortega et al. 2012). It is also suggested that an accretion disc is present, based on IR observations of de Buizer (2000). The 6.7 GHz methanol maser emission (Hu et al. 2016) is associated with a massive protostar candidate 2MASS 19142564+1109283 (Ortega et al. 2012).

#### 4.10 G45.47+0.13

OH spectra of this source show strong left-hand polarization. The NRT 1665 MHz OH spectrum shows weak right-hand polarized lines, probably resolved out by the VLA. A 1720 MHz absorption line is detected with the NRT at the systemic velocity of the source.

Left-hand polarized OH 1665 and 1667 MHz maser spots form a compact cluster with a size of  $\sim 0.2 \text{ arcsec}$  ( $\sim 1000 \text{ au}$ ). More distant OH 1667 MHz spots have positional uncertainties similar to their offsets from the central cluster.

The source is an UCH II region with a ‘possible’ bipolar outflow (Cyganowski et al. 2008). OH and 6.7 GHz methanol maser emission are detected from the same area, but it does not appear to be associated with the central continuum source (Fig. 4).

## 5 DISCUSSION

### 5.1 OH maser detection and properties of associated EGOs

The relatively low detection rate of OH masers associated with EGOs confirms the claim that our sample consists of young objects. OH masers are believed to arise in the later stages of star formation (e.g. Ellingsen et al. 2007). They are found only in 10 sources out of 20 EGOs of our initial VLA sample. In contrast, other common maser species were detected in  $\sim 90$  per cent of the sample: the detection rate of cHMM and cIMM is 95 per cent (Cyganowski et al. 2009) and H<sub>2</sub>O masers is 90 per cent (Cyganowski et al. 2013). The absence of 20-cm continuum emission in the direction of EGOs is additional evidence for their youth.

To provide context for the obtained OH maser detection rate, we compared physical parameters of two EGO subsamples: EGOs with and without OH maser detection. The summary of the parameters of the EGO subsamples is presented in Table 3. Notably, the only two ‘possible’ MYSO outflow candidates from the EGO catalogue of Cyganowski et al. (2008), G43.04–0.45 and G45.47+0.13 (EGO catalogue table 4), are both detected in the OH maser lines. In contrast to the ‘likely’ MYSO outflow candidates that form the basis of the EGO catalogue (EGO catalogue tables 1 and 2), the ‘possible’ EGOs are YSO candidates, but with less probable outflow activity. By

excluding these ‘possible’ candidates from the statistics, we obtain the OH maser detection rate of  $\sim 44$  per cent for the ‘likely’ EGOs. IRDC/non-IRDC EGOs show the same OH maser detection rate.

A significant difference in the MIR integrated flux densities was found between the EGO subsamples. EGOs detected in the OH maser lines tend to show higher MIPS 24  $\mu\text{m}$  flux densities (Multiband Imaging Photometer for Spitzer, Rieke et al. 2004) than those without OH detection (see mean value from Table 3). Moreover, the flux density of the 4.5  $\mu\text{m}$  emission is on average higher in the subsample of EGOs hosting OH masers. The mean value of the 4.5  $\mu\text{m}$  flux is three times different between OH and non-OH subsamples.

Another parameter that showed a noticeable difference between subsamples is EGO dust clump masses. Clump masses were calculated in Cyganowski et al. (2013) using the 1.1 mm Bolocam Galactic Plane Survey (BGPS) data. Comparison of masses of EGOs from our sample showed that EGOs associated with OH masers are  $\sim 3$  times less massive than clumps without OH emission.

Thus, OH maser emission appears to mark low-mass and MIR bright EGOs. Strong compact MIR emission at 24  $\mu\text{m}$  (in the absence of compact radio continuum emission) is known to characterize the later and most active stage of massive star formation (e.g. König et al. 2017). Also, for most EGOs hosting OH masers, a 24  $\mu\text{m}$  counterpart appears to be a blend of emission from multiple sources (these cases are italicized in Table 3), indicating that in these regions, more than one source has evolved enough to be bright at 24  $\mu\text{m}$ .

Note that our statistical comparison of EGO subsamples with and without OH maser detection is limited by the small sample sizes. For example, almost half of the sources of the OH maser non-detection subsample have kinematic distances of more than 10 kpc (Table 3), which reduces the probability of detecting weak OH masers in the regions. To confirm and further study the revealed patterns, it is necessary to observe a larger sample of EGOs in OH maser lines.

As is common, we found a strong correlation between the main OH lines: 90 per cent of OH(1665) masers are accompanied by weaker OH(1667) masers. The spectra of 1665/1667 MHz emission typically consist of several highly polarized lines spread over a  $\sim 10 \text{ km s}^{-1}$  velocity range. Most of the sources show a ‘twin peaks’-like spectrum, with blue- and redshifted spectral features almost symmetrically placed around the systemic source velocity.

Only two sources show OH maser emission at 1612 MHz, which – according to theoretical models (e.g. Gray et al. 1992) – is formed in less-dense and colder zones than the OH(1665) masing regions.

### 5.2 OH emission at 1720 MHz

The NRT observations found broad 1720 MHz absorption lines at the source systemic velocity in 60 per cent of the sample, that is, in six out of ten sources: G23.01–0.41, G28.83–0.25, G35.03+0.35, G35.20–0.74, G45.47+0.07, and G45.47+0.13. The linewidth of the detected absorption lines is typical for the interstellar medium (from 2 to 8  $\text{km s}^{-1}$ ).

There are several hypotheses to explain these absorption features. All our sources are associated with molecular clouds, so absorption features could arise in the interstellar medium of the Galactic spiral arms. This was the case in one of the first studies of Galactic OH absorption (Goss 1968), where absorption lines in all four OH  $\Lambda$ -doubling transitions were detected toward 26 H II regions, and OH lines approximately reflected the distribution of the H II regions in the spiral arms. On the other hand, OH absorption lines can trace bipolar outflows. For example, in the study of the well-known nearby bipolar outflow in the dark cloud L1551, Mirabel et al. (1985) and Clark &

Turner (1987) detected the OH(1665/1667) absorption lines with broad wings at the blue and red fronts of the outflow.

In our observations, OH(1720) absorption lines have no broad wings and coincide with the velocities of the parent molecular cloud (Larionov & Val'ts 2007). Close spatial association between OH and methanol masers hints that the OH(1720) absorption could arise from dense gas in the central part of the source, absorbing emission of a young stellar object.

It is also possible that with the relatively large NRT beam we observe different parts of a large molecular cloud, in which different physical conditions (temperature and density) could arise; therefore, one part of the cloud could produce emission while another produces absorption. Another possibility is that the emission and absorption arise within a single region with non-uniform physical conditions.

In cases where LTE (local thermodynamic equilibrium) is not satisfied (OH main and satellite-line intensities in our survey show non-LTE ratios), the two OH satellite lines at 1612 and 1720 MHz are known to show conjugate behaviour (one line is in absorption, while the other is in emission, see Cragg, Sobolev & Godfrey 2002; Caswell 2004), but in the absence of NRT data at 1612 MHz, we cannot verify this for our sample. Several sources (G35.03+0.35, G35.20–0.74, G45.47+0.07, and G45.47+0.13) show signs of both emission and absorption features across the 1720 MHz profile. Such spectra can be explained by the OH pumping model with non-local overlap (Litvak 1969; Lucas 1980; Pavlakis & Kylafis 1996).

OH(1720) emission lines were detected with the NRT in four sources of the EGO sample. The emission-line spectra differ significantly in these sources:

(i) G24.94+0.07 shows a weak ( $\sim 1$  Jy) broad line ( $\sim 5$  km s $^{-1}$ ) at  $\sim 53$  km s $^{-1}$ , which differs from the systemic velocity of the cloud by  $\sim 10$  km s $^{-1}$  and corresponds to the red wing of the HCO $^{+}$  line which is a bipolar outflow tracer (Cyganowski et al. 2009). It is also interesting that weak absorption ( $< 1$  Jy) is observed in the main OH lines.

(ii) G34.40+0.23 shows an even broader OH(1720) line of  $\sim 10$  km s $^{-1}$ , and is much stronger, with a flux density of  $\sim 2$  Jy. The line-centre velocity of  $\sim 60$  km s $^{-1}$  closely coincides with the systemic velocity of the EGO of  $\sim 57.63$  km s $^{-1}$  (Giannetti et al. 2014) and with the velocities of OH main lines. As noted above, this source falls into the NRT beam together with supernova remnant W44. In our VLA survey the 1720 line in the direction of W44 was detected at  $\sim 60$  km s $^{-1}$  with a flux density of  $\sim 0.7$  Jy. This line may be associated with W44 rather than G34.40+0.23.

(iii) In G35.20–0.74, two weak emission lines ( $\sim 0.5$  Jy) were detected. Both the OH emission lines and a broad absorption line are redshifted relative to the  $\sim 34$  km s $^{-1}$  systemic radial velocity of the source (Matthews et al. 1984) and fall into the red wing of the CO line (Little et al. 1983). The OH main lines show higher flux densities and are observed in the blue part of the spectrum.

(iv) G45.47+0.07 is the only source to show 1720 MHz maser emission in all our surveys. In all cases, the line shows a single peak at 62.7 km s $^{-1}$ , with strong left-hand polarization. The lowest flux density was observed in our first single-dish observation (Litovchenko et al. 2012), but was accompanied by two obvious absorption lines. The OH(1720) line closely coincides in velocity with the main OH lines ( $\Delta V \sim 2$  km s $^{-1}$ ). But all OH lines in the source are displaced by about 10 km s $^{-1}$  from the systemic velocity of the source  $\sim 56$  km s $^{-1}$  (Ortega et al. 2012) and coincide with the red wing of the  $^{13}$ CO line (Ortega et al. 2012).

The UCH II region G45.47+0.07 is at a later stage of evolution than most EGOs from our sample, which are at a very early stage,

before the appearance of an UCH II region. This fact, together with the spatial coincidence of the OH(1720) maser with the main OH lines, shows that in this case the maser is excited by a non-local line overlap mechanism. For this pumping mechanism, a significant velocity gradient in the maser region and FIR emission from dust and gas surrounding the UCH II region are necessary (Litvak 1969; Pavlakis & Kylafis 1996). Such masers are observed under conditions typical for star-forming regions (Caswell 1999), where masers are detected at the boundary between ionizing and shock fronts of UCH II.

### 5.3 OH masers' spatial distribution

The OH masers detected in the survey form clusters of  $\sim 1$ – $2$  arcsec in size. This probably exceeds the true sizes of the regions considering the positional uncertainties intrinsic to the VLA observations. Taking into account the source distances (see Table 3), such angular sizes correspond to 1000–8000 au. These values match those obtained in previous OH surveys (e.g. Caswell 1998).

No clear patterns in the OH maser spot distribution or obvious velocity gradients are found in our sample (Fig. 2). In most cases, OH(1665) maser emission comes from elongated clusters, but it is difficult to determine the spatial morphology of masers at other frequencies; in general, OH emission at 1612, 1667, and 1720 MHz shows lower flux densities and therefore higher positional uncertainties. The detected maser spots of different OH transitions are spatially coincident, that is, all OH maser species arise in the same region. Combined OH emission often seems to form extended, halo-like structures (Fig. 4).

OH maser emission is found in the vicinity of compact sources traced by 24  $\mu$ m (Cyganowski et al. 2009) or C-band continuum (Hu et al. 2016) emission in 60 per cent of the sample (see Fig. 4). In the remaining cases, OH maser emission is more likely associated with another source in the field (see Section 4). For example, in EGO G34.40+0.23, OH maser emission is detected in MYSO G34.4+0.23 MM1 (Rathborne et al. 2006), while C-band continuum emission (Hu et al. 2016) is associated with UCH II region G34.4+0.23 MM2 (Rathborne et al. 2006).

Only two sources of the sample do not have a 6.7 GHz methanol maser counterpart: G34.4+0.23 and G45.47+0.07 (Fig. 4). Theoretical models show that the 6.7 GHz methanol and OH masers arise under very similar excitation conditions, and excitation of only one type of maser is a rather rare case (Cragg et al. 2002). In general, the absence of maser emission at 6.7 GHz means that methanol molecules are not widely abundant in a region hosting an OH maser (Cragg et al. 2002). Remarkably, both sources show OH satellite-line emission: OH(1612) maser is detected in G34.4+0.23 and OH(1720) maser is detected in G45.47+0.07. The absence of 6.7 GHz methanol maser emission at the OH maser site in G45.47+0.07 contradicts general statistics; OH maser surveys (e.g. Caswell 1999) revealed an absolute correlation between OH 1720 MHz satellite-line maser sites and 6.7 GHz methanol masers. The OH 1720 MHz and 6.7 GHz methanol masers occur under the same conditions according to theoretical models (Cragg et al. 2002). In contrast, it is expected that methanol maser emission will not be detected towards the site of 1612 MHz emission. The OH 1612 MHz maser emission occurs under warm gas conditions, which are not suitable for ensuring a sufficient methanol abundance (Cragg et al. 2002). It is believed that OH 1612 MHz maser emission and absence of 6.7 GHz methanol maser emission signifies an advanced stage of star-forming region evolution (Caswell 1999).

In most cases, the OH maser emission closely coincides with the positions of the 6.7 GHz methanol masers. The 6.7 GHz methanol

masing region is generally  $\sim 2$ – $3$  times more compact than the OH maser cluster (Fig. 4). However, there are several exceptions. Sources G35.20–0.74 and G43.04–0.45 show elongated 6.7 GHz methanol maser clusters atypical for our sample, and similar in size to OH emitting regions. While the OH maser emission follows the structure of the 6.7 GHz methanol maser cluster in G35.20–0.74, the OH maser region in G43.04–0.45 shows no organized structure and is associated with the north lobe of the 6.7 GHz methanol maser cluster. OH and methanol maser emission in G35.20–0.74 is thought to be associated with a Keplerian rotating disc (Sánchez-Monge et al. 2013). Sizes of both OH and 6.7 GHz methanol maser sites are similar in two sources: G19.36–0.03 and G45.47+0.13. The latter source, along with G35.03+0.35 and G43.04–0.45, is part of a group of objects in which the OH and 6.7 GHz methanol masers are near to one another, but do not coincide exactly.

No clear evidence of association between OH maser emission and shocked outflow gas traced by 44 GHz methanol maser emission is found. The detected OH maser emission originates near the central sources of the EGOs and is associated with the base of an outflow. OH maser emission coexists with the 6.7 GHz methanol maser emission, but is found in larger and more diffuse clusters.

#### 5.4 OH line polarimetry

All the sources detected in our survey exhibit circularly polarized OH emission, while linearly polarized features are found in 80 per cent of OH(1665) and less than 50 per cent of OH(1667). Since linear polarization in the detected lines is always associated with some degree of circular polarization, we conclude that only elliptically polarized emission was found.

From the NRT polarimetric data analysis, we identified those OH maser features with linear polarization emission and determined their polarization angles (Table 4). The orientation of linear polarization vectors can be used to determine the magnetic field orientation within the region (e.g. Surcis et al. 2012). The quality of our data does not allow us to conduct a reliable analysis of orientation of the magnetic field in the sources, but we try to test it with obtained values of linear polarization vectors (Table 4). The directions of linear polarization vectors is expected to be parallel or perpendicular to the magnetic field direction (Goldreich, Keeley & Kwan 1973). Since the linear polarization of the detected OH masers most probably arises from the elliptical polarization of the  $\sigma$ -components, here we consider the polarization angle to be perpendicular to the magnetic field. Note that in our analysis we use this simple assumption and do not follow the polarization fitting procedure described in Surcis et al. (2011). In four sources (G19.36–0.04, G23.01–0.41, G28.83–0.25, and G35.20–0.74), the magnetic field is oriented along the outflows in EGOs, similar to the results of Surcis et al. (2015) who found that the magnetic field was preferentially aligned with the outflow axis.

Low spatial resolution of the VLA observations prevented us from identification of Zeeman pairs and analysing magnetic fields in the sources. In order to find Zeeman patterns, groups of OH maser features with opposite circular polarization that coincide spatially need to be identified. Ideally, components of a Zeeman pair should coincide on the sky to better than the OH maser spot size (Fish et al. 2003). Using the positional uncertainty estimate from Reid et al. (1980) shows that OH masers in W3(OH) cluster on a scale of  $3 \times 10^{15}$  cm and that oppositely circularly polarized maser lines within the cluster give a reliable magnetic field measurement when interpreted as Zeeman pairs. EGOs from our sample are located at distances from 1.56 to 8.40 kpc (see Table 3). At these distances, 200 au corresponds to angular sizes of 0.13 and 0.024 arcsec, respectively.

These angular sizes are smaller than the positional uncertainties achieved in our survey, that is, we cannot use this restriction to test the identified Zeeman pairs. The study of magnetic fields at au scales requires high-resolution VLBI (very long baseline interferometry) data, and as a next step of our study, we perform VLBI polarization mapping observations of OH masers in the direction of several EGOs of our sample.

## 6 CONCLUSIONS

We find a relatively low detection rate of OH masers associated with EGOs. OH emission is detected in 50 per cent of the EGO sample and in only 44 per cent of the ‘likely’ EGOs. Together with the non-detection of 20-cm continuum emission toward the sample, this indicates that most EGOs are in the earliest stages of MYSO evolution.

EGOs hosting OH masers were found to exhibit brighter MIPS 24  $\mu$ m and IRAC 4.5  $\mu$ m emission than those without OH masers. Moreover, EGOs with OH masers have lower dust clump masses.

VLA and NRT polarization data for 10 EGOs is presented. OH maser emission forms extended, halo-like clusters of size of  $\sim 1$  arcsec (several thousand au depending on the distance to the source). Detected OH maser emission originates near central sources of EGOs and is associated with the base of an outflow. OH maser emission coexists with the 6.7 GHz methanol masers, but is found in larger and more diffuse clusters.

NRT observations reveal the presence of broad thermal absorption OH(1720) lines in the direction of four EGOs. Preliminary analysis of linear polarization angles orientation shows that in  $\sim 50$  per cent of sources the directions of the magnetic field and the outflow are most likely parallel.

## ACKNOWLEDGEMENTS

We are deeply grateful to our dear colleague, good friend, and brilliant scientist G. M. Rudnitskij who passed away shortly before finishing work on this paper.

We thank G. M. Larionov for help with the data reduction and paper preparation.

## DATA AVAILABILITY

The data underlying this article are accessible from the NRAO Science Data Archive (<https://archive.nrao.edu/>) with the data set identifier 13A-406. The derived data generated in this research will be shared upon reasonable request to the corresponding author.

## REFERENCES

- Araya E. D., Hofner P., Goss W. M., Linz H., Kurtz S., Olmi L., 2008, *ApJS*, 178, 330  
 Bally J., Zinnecker H., 2005, *AJ*, 129, 2281  
 Bayandina O. S., Alakoz A. V., Val’tts I. E., 2013, *Aston. Rep.*, 57, 889  
 Bayandina O. S., Val’tts I. E., Kurtz S. E., 2015, *Aston. Rep.*, 59, 998  
 Beltrán M. T. et al., 2014, *A&A*, 571, A52  
 Beltrán M. T., Cesaroni R., Moscadelli L., Sánchez-Monge Á., Hirota T., Kumar M. S. N., 2016, *A&A*, 593, A49  
 Benjamin R. A. et al., 2003, *PASP*, 115, 953  
 Bonnell I. A., Bate M. R., Zinnecker H., 1998, *MNRAS*, 298, 93  
 Brebner G. C., Heaton B. D., Cohen R. J., Davies S. R., 1987, *MNRAS*, 229, 679  
 Caswell J. L., 1998, *MNRAS*, 297, 215

- Caswell J. L., 1999, *MNRAS*, 308, 683
- Caswell J. L., 2004, *MNRAS*, 349, 99
- Chen X., Shen Z.-Q., Li J.-J., Xu Y., He J.-H., 2010, *ApJ*, 710, 150
- Chen X., Gan C.-G., Ellingsen S. P., He J.-H., Shen Z.-Q., Titmarsh A., 2013, *ApJS*, 206, 9
- Churchwell E. et al., 2006, *ApJ*, 649, 759
- Churchwell E. et al., 2009, *PASP*, 121, 213
- Clark B. G., 1980, *A&A*, 89, 377
- Clark F. O., Turner B. E., 1987, *A&A*, 376, 114
- Codella C., Testi L., Cesaroni R., 1997, *A&A*, 325, 282
- Cortes P. C., Crutcher R. M., Shepherd D. S., Bronfman L., 2008, *ApJ*, 676, 464
- Cragg D. M., Sobolev A. M., Godfrey P. D., 2002, *MNRAS*, 331, 521
- Cyganowski C. J. et al., 2008, *AJ*, 136, 2391
- Cyganowski C. J., Brogan C., Hunter T. R., Churchwell E., 2009, *ApJ*, 702, 1615
- Cyganowski C. J., Brogan C. L., Hunter T. R., Churchwell E., 2011a, *ApJ*, 743, 56
- Cyganowski C. J., Brogan C. L., Hunter T. R., Churchwell E., Zhang Q., 2011b, *ApJ*, 729, 124
- Cyganowski C. J., Koda J., Rosolowsky E., Towers S., Meyer D., Egusa F., Momose R., Robitaille T. P., 2013, *ApJ*, 764, 61
- De Buizer J., 2000, PhD thesis, University of Florida, available at <http://www.jim-debuizer.net/thesis.pdf>
- De Buizer J. M., Vacca W. D., 2010, *AJ*, 140, 196
- de Villiers H. M. et al., 2014, *MNRAS*, 444, 566
- Dent W. R. F., Little L. T., Kaifu N., Ohishi M., Suzuki S., 1985, *A&A*, 146, 375
- Edris K. A., Fuller G. A., Cohen R. J., 2007, *A&A*, 465, 865
- Edris K. A., Fuller G. A., Etoka S., Cohen R. J., 2017, *A&A*, 608, A80
- Elitzur M., 1992, *ARA&A*, 30, 75
- Ellingsen S. P., Voronkov M. A., Cragg D. M., Sobolev A. M., Breen S. L., Godfrey P. D., 2007, in Chapman J. M., Baan W. A., eds, *IAU Symp. 242, Astrophysical Masers and their Environments*. Cambridge Univ. Press, Cambridge, p. 213
- Fazio G. G. et al., 2004, *ApJS*, 154, 10
- Fish V. L., Reid M. J., Argon A. L., Menten K. M., 2003, *ApJ*, 596, 328
- Furuya R. S., Cesaroni R., Takahashi S., Codella C., Momose M., Beltrán M. T., 2008, *ApJ*, 673, 363
- Garay G., Lizano S., 1999, *PASP*, 111, 1049
- Giannetti A. et al., 2014, *A&A*, 570, A65
- Goldreich P., Keeley D. A., Kwan J. Y., 1973, *ApJ*, 179, 111
- Goss W. M., 1968, *ApJS*, 15, 131
- Gray M. D., Field D., Doel R. C., 1992, *A&A*, 262, 555
- He J. H., Takahashi S., Chen X., 2012, *ApJS*, 202, 1
- Heckman T. M., Thompson T. A., 2017, in Alsabti A., Murdin P., eds, *Handbook of Supernovae*. Springer, Cham
- Hu B., Menten K. M., Wu Y., Bartkiewicz A., Rygl K., Reid M. J., Urquhart J. S., Zheng X., 2016, *ApJ*, 833, 18
- König C. et al., 2017, *A&A*, 599, A139
- Larionov G. M., Val'ts I. E., 2007, *Astron. Rep.*, 51, 756
- Lee H.-T., Takami M., Duan H.-Y., Karr J., Su Y.-N., Liu S.-Y., Froebrich D., Yeh C. C., 2012, *ApJS*, 200, 2
- Lee H.-T. et al., 2013, *ApJS*, 208, 23
- Litovchenko I. D. et al., 2012, *Astron. Rep.*, 56, 536
- Little L. T., Brown A. T., Riley P. W., Matthews N., Macdonald G. H., Vizard D. R., Cohen R. J., 1983, *MNRAS*, 203, 409
- Little L. T., Dent W. R. F., Heaton B. D., Davies S. R., White G. J., 1985, *MNRAS*, 217, 227
- Litvak M. M., 1969, *ApJ*, 156, 471
- Lucas R., 1980, *A&A*, 84, 36
- Matthews N., Little L. T., Nyman L. A., Macdonald G. H., 1984, *A&A*, 136, 282
- McKee C. F., Tan J. C., 2003, *ApJ*, 585, 850
- McMullin J. P., Waters B., Schiebel D., Young W., Golap K., 2007, in Shaw R. A., Hill F., Bell D. J., eds, *ASP Conf. Ser. Vol. 376, Astronomical Data Analysis Software and Systems XVI*. Astron. Soc. Pac., San Francisco, p. 127
- Mirabel I. F., Rodríguez L. F., Cantó J., Arnal E. M., 1985, *ApJ*, 294, L39
- Ortega M. E., Paron S., Cichowolski S., Rubio M., Dubner G., 2012, *A&A*, 546, A96
- Paron S., Weidmann W., 2010, *MNRAS*, 408, 2487
- Pavlakis K. G., Kylafis N. D., 1996, *ApJ*, 467, 309
- Rathborne J. M., Jackson J. M., Simon R., 2006, *ApJ*, 641, 389
- Reach W. T. et al., 2006, *AJ*, 131, 1479
- Reid M. J., Haschick A. D., Burke B. F., Moran J. M., Johnston K. J., Swenson G. W., Jr, 1980, *ApJ*, 239, 89
- Reid M. J., Schneps M. H., Moran J. M., Gwinn C. R., Genzel R., Downes D., Ronnang B., 1988, *ApJ*, 330, 809
- Rieke G. H. et al., 2004, *ApJS*, 154, 25
- Rudnitskii G. M., Lekht E. E., Bayandina O. S., Val'ts I. E., Khan E. R., 2016, *Astron. Rep.*, 60, 129
- Sánchez-Monge Á. et al., 2013, *A&A*, 552, L10
- Sanna A., Moscadelli L., Cesaroni R., Tarchi A., Furuya R. S., Goddi C., 2010, *A&A*, 517, A78
- Shepherd D. S., Nurnberger D. E. A., Bronfman L., 2004, *ApJ*, 602, 850
- Shepherd D. S., Povich M. S., Whitney B. A., Robitaille T. P., 2007, *ApJ*, 669, 464
- Shu F. H., Adams F. C., Lizano S., 1987, *ARA&A*, 25, 23
- Slysh V. I., Pashchenko M. I., Rudnitskij G. M., Vitrichchak V. M., Colom P., 2010, *Astron. Rep.*, 54, 599
- Surcis G., Vlemmings W. H. T., Curiel S., Hutawarakorn Kramer B., Torrelles J. M., Sarma A. P., 2011, *A&A*, 527, A48
- Surcis G., Vlemmings W. H. T., van Langevelde H. J., Hutawarakorn Kramer B., 2012, *A&A*, 541, A47
- Surcis G., Vlemmings W. H. T., van Langevelde H. J., Hutawarakorn Kramer B., Bartkiewicz A., Blasi M. G., 2015, *A&A*, 578, A102
- Szymczak M., Gerard E., 2004, *A&A*, 423, 209
- Towner A. P. M., Brogan C. L., Hunter T. R., Cyganowski C. J., McGuire B. A., Indebetouw R., Friesen R. K., Chandler C. J., 2017, *ApJS*, 230, 22
- Varricatt W. P., Davis C. J., Ramsay S., Todd S. P., 2010, *MNRAS*, 404, 661
- Watson C. et al., 2008, *ApJ*, 681, 1341
- Wood D. O. S., Churchwell E., 1989, *ApJS*, 69, 831
- Wu Y. W. et al., 2014, *A&A*, 566, A17
- Zhang B., Zheng X. W., Reid M. J., Menten K. M., Xu Y., Moscadelli L., Brunthaler A., 2009, *ApJ*, 693, 419
- Zhang Q., Hunter T. R., Brand J., Sridharan T. K., Cesaroni R., Molinari S., Wang J., Kramer M. A., 2005, *ApJ*, 625, 864
- Zinnecker H., Yorke H. W., 2007, *ARAA*, 45, 481

## SUPPORTING INFORMATION

Supplementary data are available at [MNRAS](https://academic.oup.com/mnras/article/499/3/3961/5909618) online.

**Table S2.** OH maser parameters obtained with the VLA in the EGO sample.

**Figure 1.** Spectra of EGO sources obtained with VLA and NRT.

**Figure 2.** Fitted positions and cross-correlation spectra of OH masers detected with VLA.

**Figure 3.** Profiles of Stokes parameters, degree of polarization, and polarization angle for the OH lines obtained with NRT in the direction of the EGO sample.

**Figure 4.** Combined maps of objects of the studied EGO sample.

Please note: Oxford University Press is not responsible for the content or functionality of any supporting materials supplied by the authors. Any queries (other than missing material) should be directed to the corresponding author for the article.

This paper has been typeset from a  $\text{\TeX}/\text{\LaTeX}$  file prepared by the author.